KRONOS FUSION ENERGY

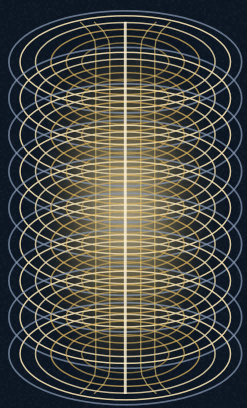

PAPER 2.18 · THE KRONOS 2026 SERIES

First-Principles Radiation Tolerance of Centrepost REBCO in a Compact Spherical-Tokamak Breeder: Chain-Oxygen-Vacancy Formation by DFT+U and YBCO Displacement-Cascade Molecular Dynamics

The consumable centrepost of the Hyperion breeder carries the machine's peak field of T inside its harshest neutron environment, so the irradiation lifetime of the centrepost…

Read it live — 3-D model · physics validator · film series

BY P I FORD, R J WEGGEL AND C WEGGEL

2026 · EDITORIAL EDITION

THE OFFICIAL RECORD

What this document is, and how to read its numbers

This is a combined editorial. It gathers, in one volume, the two design studies Kronos Fusion Energy released in 2026 — a compact spherical-tokamak tritium/helium-3 breeder and a deuterium–helium-3 tandem-mirror generator — together with the intellectual-property estate, the people, and, in the internal edition, the full commercial case. The scientific text is the same text that appears in the arXiv preprints and the journal submissions; the editorial adds the apparatus a reader needs to hold the whole program at once, and nothing in the physics is altered to fit it.

THE HONESTY STANCE IS THE ASSET

Every headline quantity carries an **evidence class** — DERIVED RECOMPUTED MEASURED REQUIREMENT — and, where a number is a modelled extrapolation rather than a demonstrated value, it is labelled as such and its downside is shown next to it. Several quantities in the underlying corpus moved after first publication; where a value has been withdrawn or restated, the record says so plainly. This is deliberate: a diligence team will find the load-bearing assumptions, so the document surfaces them first.

TWO EDITIONS

This volume is issued in two editions. The **public edition** (light) carries the physics and the design only — no dollar, price, or per-kilogram figure appears anywhere in it. The **internal edition** (dark) adds the economics, the funding architecture, and the defense-commercial analysis, and is marked *Confidential* accordingly; it is not for public distribution. Where the commercial case rests on a modelled assumption rather than a demonstrated one, it is labelled as such and its downside is shown alongside it, on the same terms as the physics.

TITLE	The Kronos Fleet — Hyperion · Aegis · MetroVolt: A Combined Design & Commercialization Study
AUTHOR	Priyanca Ford, Founder & CEO, on behalf of Kronos Fusion Energy
EDITION	2026 Combined Editorial · first issue
COMPANION WORKS	The five-paper arXiv drop — (1) Breeder, (2) Burner, (3) REBCO magnet & tape, (4) Direct Energy Conversion, (5) AI/ML/Quantum control — with matching numbered Zenodo deposits, plus the IOP journal and IAEA-FEC submissions. Patents were filed before the drop.
NAMING	Hyperion = the breeder; Aegis (defense) and MetroVolt (data-center) = one generator in two housings. Internal mode letters (D1, L) do not appear on public surfaces.
STATUS	Conceptual design & simulation study. Nothing herein is a construction commitment.

HOW TO READ THIS VOLUME

The fleet at a glance, and the way its numbers are marked

This volume opens with *Orientation*, presents the five research papers as a bound sequence, and closes with the *Apparatus*. *Foundations* sets out the three general results both machines rest on. *Paper One* is the Hyperion breeder; *Paper Two* the Aegis / MetroVolt generator; *Papers Three, Four and Five* are the enabling science — high-field REBCO magnets and tape, direct energy conversion, and the AI / ML / quantum control stack. A *Digital Twin & 3-D Model* part follows, then the *Environmental* profile. The *Economics* and levelized cost and the *Business Case* and diligence record appear in the internal edition only; the *Simulations* proof record and the Apparatus — patent portfolio, team, limitations, and sources — close both editions.

THE FLEET AT A GLANCE

	HYPERION	AEGIS	METROVOLT
Role	Strategic-isotope foundry	Defense installation power	Campus power
Machine	**Spherical tokamak**	**Tandem mirror**	**Tandem mirror**
Fuel	Deuterium–tritium	Deuterium–helium-3	Deuterium–helium-3
Delivers	Tritium · ^{3}He · 14 MeV n	Resilient installation power	Firm campus power
Physics bar	**Fusion gain only**	Closure (gates named)	Closure + lunar ^{3}He
In the fleet	Breeds the fuel	Proves the generator	Commercial destination

HOW THE NUMBERS ARE MARKED

Every headline quantity carries an evidence class — DERIVED from first principles, RECOMPUTED from raw data, MEASURED in hardware, or a REQUIREMENT yet to be met. Financial figures carry a case label and are confined to the internal (confidential) edition. Values that moved after first publication are shown as withdrawn or restated rather than quietly changed. A capability you can evaluate is one whose limits are on the page.

ABSTRACT

First-Principles Radiation Tolerance of Centrepost REBCO in a Compact Spherical-Tokamak Breeder: Chain-Oxygen-Vacancy Formation by DFT+U and YBCO Displacement-Cascade Molecular Dynamics

The consumable centrepost of the Hyperion breeder carries the machine's peak field of 16.84 T inside its harshest neutron environment, so the irradiation lifetime of the centrepost REBCO conductor—not stress and not quench—sets the cadence at which the plant is opened and, through it, the fraction of the calendar available for power production. We pose the lifetime question as a coupled multiscale problem and solve it from first principles. Steady 14 MeV neutron transport supplies the fast-flux field and the primary-knock-on-atom (PKA) spectrum at the conductor; a displacement-cascade molecular-dynamics (MD) treatment with a machine-learned interatomic potential and an arc-dpa surviving-defect model converts that spectrum into Frenkel-pair statistics resolved by sublattice; a DFT+U treatment of the correlated Cu $3d$/O $2p$ manifold fixes the chain-oxygen-vacancy energetics; and a hole-doping dome maps chain-oxygen loss onto the critical temperature and current. A Monte-Carlo composition screen over $4{,}000$ samples spanning the material and irradiation-model uncertainties finds that an *un-doped* YBCO tape reaches its critical-current break-even fluence at $\Phi^* = 5.64 \times 10^{22}\,\mathrm{n\,m^{-2}}$—a factor of 1.48 above the artificial-pinning-center (APC) grade at $3.82 \times 10^{22}\,\mathrm{n\,m^{-2}}$—and the ordering un-doped $>$ APC is robust in $100\,\%$ of the samples. The displacement analysis localises $\approx 78\,\%$ of surviving lattice displacements on the oxygen sublattice, naming chain-oxygen disorder as the dominant lifetime-limiting channel; and a converged DFT+U calculation of the pristine cell ($E_{\mathrm{tot}} = -2907.082$ Ry) anchors the chain-oxygen-vacancy formation-energy series from a validated ground state. We report the governing equations, the numerical formulation, and the GPU high-performance-computing (HPC) campaign that produced the results, and we close with the one honest reconciliation the design must carry: the break-even-fluence ranking (radiation tolerance) is a distinct metric from the end-of-life in-field I_c margin at the full 16.84 T operating point, and the two are separated cleanly rather than conflated. The centrepost gains a physically grounded, conservative irradiation-lifetime basis whose engineering lever is oxygen-sublattice integrity, not pinning-center density.

Open-access deposit (code & data, CC BY 4.0): DOI 10.5281/zenodo.22645923 · Zenodo community *kronos_fusion_energy*. Explore it live: interactive 3-D model · physics validator.

Keywords: REBCO · YBCO · radiation damage · DFT+U · displacement cascade · oxygen vacancy · critical current · spherical-tokamak centrepost

CONTENTS

Table of Contents

NOMENCLATURE

Symbols, units, and the names of things

Q	plasma (fusion) gain, P_{fus}/P_{aux}
Q_E	engineering gain, net electric out / recirculating in
H_{98}	confinement enhancement over the IPB98(y,2) scaling
Z_{eff}	effective ion charge
c_{ee}	electron–electron bremsstrahlung leading coefficient, 2.120022 (exact)
τ_E	energy confinement time
I_p	plasma current
R_0, a	major radius, minor radius
κ, δ	elongation, triangularity
β_N	normalized plasma beta (Troyon-normalized)
TBR	tritium breeding ratio
DEC	direct energy conversion
CF	plant capacity factor (availability)
FOAK / NOAK / BOAK	first / n^{th} / best of a kind
Hyperion	the ST breeder (internal: Mode D2)
Aegis	the generator, defense/installation housing (internal: Mode M)
MetroVolt	the generator, data-center housing (Mode M)

§ 1

Introduction

The Hyperion breeder is a compact, high-field spherical tokamak (ST) whose central column is a demountable REBCO centrepost operating at a peak field of 16.84 T, behind a plasma of $I_p = 9.66$ MA at major radius $R_0 = 1.20$ m, aspect ratio $A = 2.5$, elongation $\kappa = 2.0$ and negative triangularity $\delta = -0.30$, delivering $Q = 3.076$ at $P_{\text{fus}} = 85.04$ MW. The centrepost sits closest to the 14 MeV source and absorbs the highest neutron fluence of any magnet in the plant. Because the column is designed to be swapped rather than to last the plant lifetime, its *irradiation lifetime* is not a reliability footnote: it is the quantity that sets how often the machine is opened, and thus the availability envelope of the whole plant.

The governing question is quantitative and material. At what fast-neutron fluence does the conductor's critical current fall to the design break-even point, and what physical process drives that decline? The two parts of the question are coupled: an actionable lifetime number is only as good as the mechanism behind it, because the mechanism names the design lever. This paper answers both, from electronic structure and atomistic simulation up to a lifetime figure of merit, and it does so for the specific conductor and field of the Hyperion centrepost.

PRIOR ART

REBCO (rare-earth barium copper oxide; here $YBa_2Cu_3O_{7-\delta}$, “YBCO”) retains a high critical-current density in high field, which is why it is the enabling conductor for compact high-field magnets in the ARC and SPARC line of high-field tokamaks and for the ST pilot-plant class [2,3,1]. The coated-conductor manufacturing base has matured to the current densities and volumes a fusion magnet demands [4,5], and record dc fields above 45 T have been demonstrated with no-insulation REBCO windings [6]. Fast-neutron irradiation degrades the in-field critical current of these conductors by introducing point defects and disorder that both suppress the superconducting order parameter and rearrange the flux-pinning landscape [10,11,12]. The engineering figure of merit is the *break-even fluence*: the accumulated fast-neutron fluence at which the irradiated critical current drops to the design floor.

Commercial REBCO is frequently supplied with *artificial pinning centers* (APC)—engineered nanoscale $BaZrO_3$/$BaHfO_3$ inclusions that raise the in-field critical current in the pristine state [8,9,7]. The design question is whether that pristine advantage survives irradiation, or whether the added disorder consumes the radiation-tolerance budget faster than it raises the starting current. We resolve this by direct comparison, and we anchor the resolution in the mechanism.

On the electronic-structure side, YBCO's superconductivity is controlled by charge transfer from the Cu–O chains to the CuO_2 planes, so the oxygen content of the chains sets the hole doping and hence the critical temperature [13,14,15]. A correlated-electron treatment is required: the Cu $3d$/O $2p$ manifold is mishandled by a plain generalised-gradient functional, and the Hubbard-corrected DFT+U method is the standard first-principles remedy [17,18,19]. On the damage-production side, the connection from a neutron field to a displacement count runs through the Norgett– Robinson–Torrens (NRT) standard and its modern arc-dpa correction for athermal in-cascade recombination [24,25], evaluated on cascades computed by large-scale molecular dynamics [23,26] with interatomic forces from machine-learned potentials [27,28,29] trained on first-principles data.

CONTRIBUTION

This paper is the first-principles complement to the centrepost magnet-integrity case. That case establishes that the column is structurally sound with a large margin and thermally stable, so the neutron budget of the conductor is the governing lifetime term rather than stress or quench [32,33]; the present work supplies the physical content of that budget. Three results move together. (i) A $4{,}000$-sample composition screen shows the un-doped grade is $1.48\times$ more radiation-tolerant than the APC grade on the break-even-fluence metric, and the ordering is universal. (ii) The damage is localised on the oxygen sublattice at $\approx 78\,\%$ of surviving displacements, so the lifetime-limiting mechanism is chain-oxygen disorder. (iii) The mechanism is anchored at the electronic-structure level by a converged DFT+U ground state, from which the chain-oxygen-vacancy energetics are referenced. We state each result as the output of an explicit governing model (§3) solved by a named GPU-HPC campaign (§4), and we place the numbers against the published irradiation literature (§6). The companion papers develop the conductor and winding basis [31], the un-doped-tape rule in the broader stabilizer context [34], the fast-fluence/dpa/shielding neutronics that set the flux [33], the fluence-driven remaining-useful-life scheduling [36], and the machine-learned-potential-to-transport materials pipeline whose methods this paper shares [37].

Two distinct magnets appear in the Kronos fleet and must not be conflated: the breeder centrepost analysed here, governed by its own 16.84 T peak field, and the burner plug coil at 26.49 T, engineered separately [39]. All results below refer to the centrepost conductor.

§ 2

The centrepost lifetime problem

The centrepost is a demountable, radially thin REBCO winding forming the inboard leg of the toroidal-field circuit of a low-aspect-ratio ST. Its physical predicament is geometric: at $A = 2.5$ and $R_0 = 1.20\,\mathrm{m}$ the inboard radial build is severely constrained, so the neutron shield between the plasma and the conductor is thin, and the fast flux at the winding is a small but non-negligible fraction of the first-wall value. The first wall itself sees $19.66\,\mathrm{dpa\,fpy^{-1}}$ under $14\,\mathrm{MeV}$ loading [38]; the centrepost, behind its shield, accumulates a far lower displacement rate, but over a full-power year it is enough to be the binding lifetime constraint of the machine [33,40].

The design response is to make the column consumable: a cartridge that is swapped on a defined cadence rather than qualified for the plant lifetime. That choice converts a materials-survival problem into a scheduling problem, and it makes the break-even fluence Φ^* the single most consequential conductor property, because the swap cadence is $\nu_{\mathrm{swap}} = 1/\tau$ with lifetime $\tau = \Phi^*/\bar{\phi}$ at the mean centrepost fast flux $\bar{\phi}$. A larger Φ^* is a longer-lived centrepost, a lower cadence, and a higher plant availability. Everything in this paper is organised around computing Φ^* for two candidate grades and understanding the mechanism that sets it.

§ 3

Governing equations and the formal problem

We formalise the lifetime problem as a chain of five coupled models, sketched in Figure 1: damage production, cascade partition, chain-oxygen accumulation, electronic structure, and the critical-current response. The break-even fluence is the functional of these that the composition screen samples.

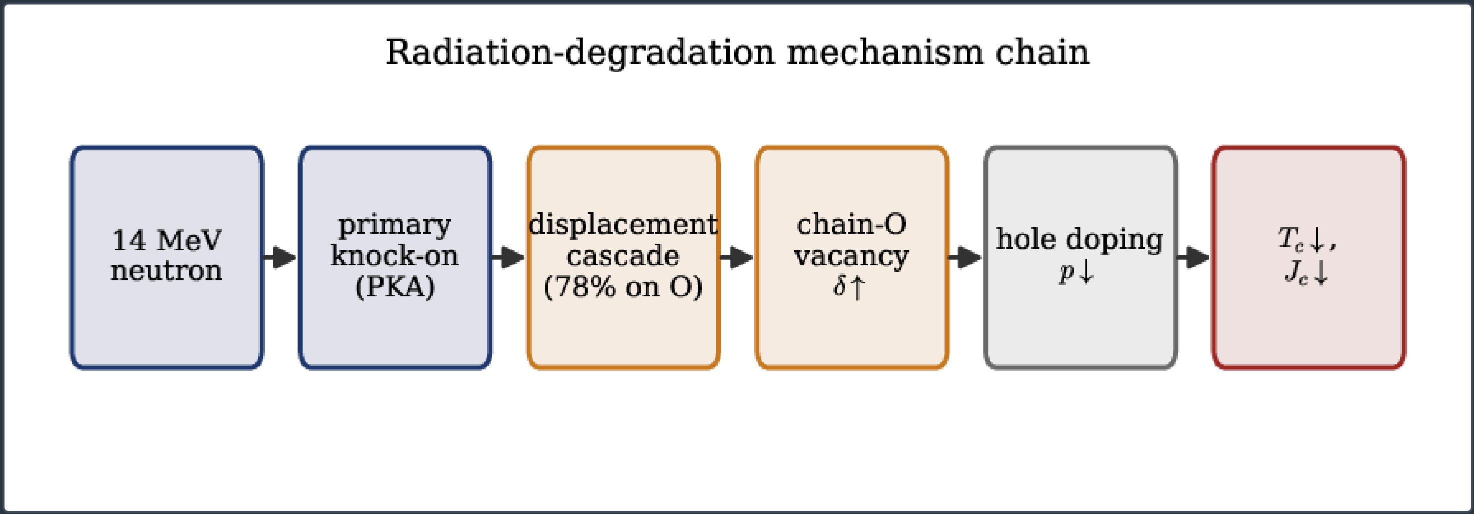

(Schematic.) The radiation-degradation mechanism chain for the centrepost conductor. A 14 MeV neutron produces a primary knock-on atom; the ensuing displacement cascade deposits $\approx 78\,\%$ of its surviving displacements on the oxygen sublattice; chain-oxygen vacancies raise the vacancy fraction δ; the CuO-chain charge reservoir loses holes ($p\downarrow$); and T_c and J_c fall. Each arrow is one governing model in §3.

DAMAGE SOURCE: TRANSPORT, PKA SPECTRUM AND THE NRT/ARC-DPA COUNT

Let $\phi(E, \quad r)$ be the steady fast-neutron scalar flux at conductor position $\quad r$, obtained from the transport of the 14 MeV source through the inboard shield. The atomic displacement rate is the flux folded with the displacement cross-section,

$$R_d(\quad r) = \int_{E_{\min}}^{E_{\max}} \phi(E, \quad r)\,\sigma_d(E)\,\mathrm{d}E, \qquad \sigma_d(E) = \int_0^{T_{\max}(E)} \frac{\mathrm{d}\sigma}{\mathrm{d}T}(E\to T)\,\nu(T)\,\mathrm{d}T,$$

where T is the primary-knock-on-atom (PKA) recoil energy, $\mathrm{d}\sigma/\mathrm{d}T$ the recoil kernel and $\nu(T)$ the number of stable displacements produced by a PKA of energy T. The NRT standard [24] writes the displacement number through the Lindhard damage-partition energy $T_{\mathrm{dam}}(T) = T/[1 + k\,g(\varepsilon)]$, which removes the fraction of the PKA energy lost to electronic excitation,

$$\nu_{\mathrm{NRT}}(T) = \begin{cases} 0, & T_{\mathrm{dam}} < E_d, \\ 1, & E_d \le T_{\mathrm{dam}} < 2E_d/0.8, \\ \dfrac{0.8\,T_{\mathrm{dam}}(T)}{2E_d}, & T_{\mathrm{dam}} \ge 2E_d/0.8, \end{cases}$$

with E_d the effective threshold displacement energy of the recoiling sublattice. The NRT count over-predicts the number of *surviving* defects because it ignores athermal in-cascade recombination; the arc-dpa model [25] multiplies by an energy-dependent surviving-defect efficiency $\xi(T) = \big(1 - c_{\mathrm{arc}}\big)T_{\mathrm{dam}}^{b_{\mathrm{arc}}} + c_{\mathrm{arc}}$, so the surviving displacement count is $\nu(T) = \xi(T)\,\nu_{\mathrm{NRT}}(T)$ (Figure 2). The accumulated damage after exposure time t is $D(\quad r, t) = R_d(\quad r)\,t$, and the fast fluence is $\Phi(\quad r, t) = \int_0^t \int_{0.1\,\mathrm{MeV}}^{\infty} \phi(E, \quad r)\,\mathrm{d}E\,\mathrm{d}t'$; the two are proportional at the fixed spectral shape of the shielded centrepost, $D = \Lambda\,\Phi$, with Λ the fluence-to-dpa conversion returned by 1.

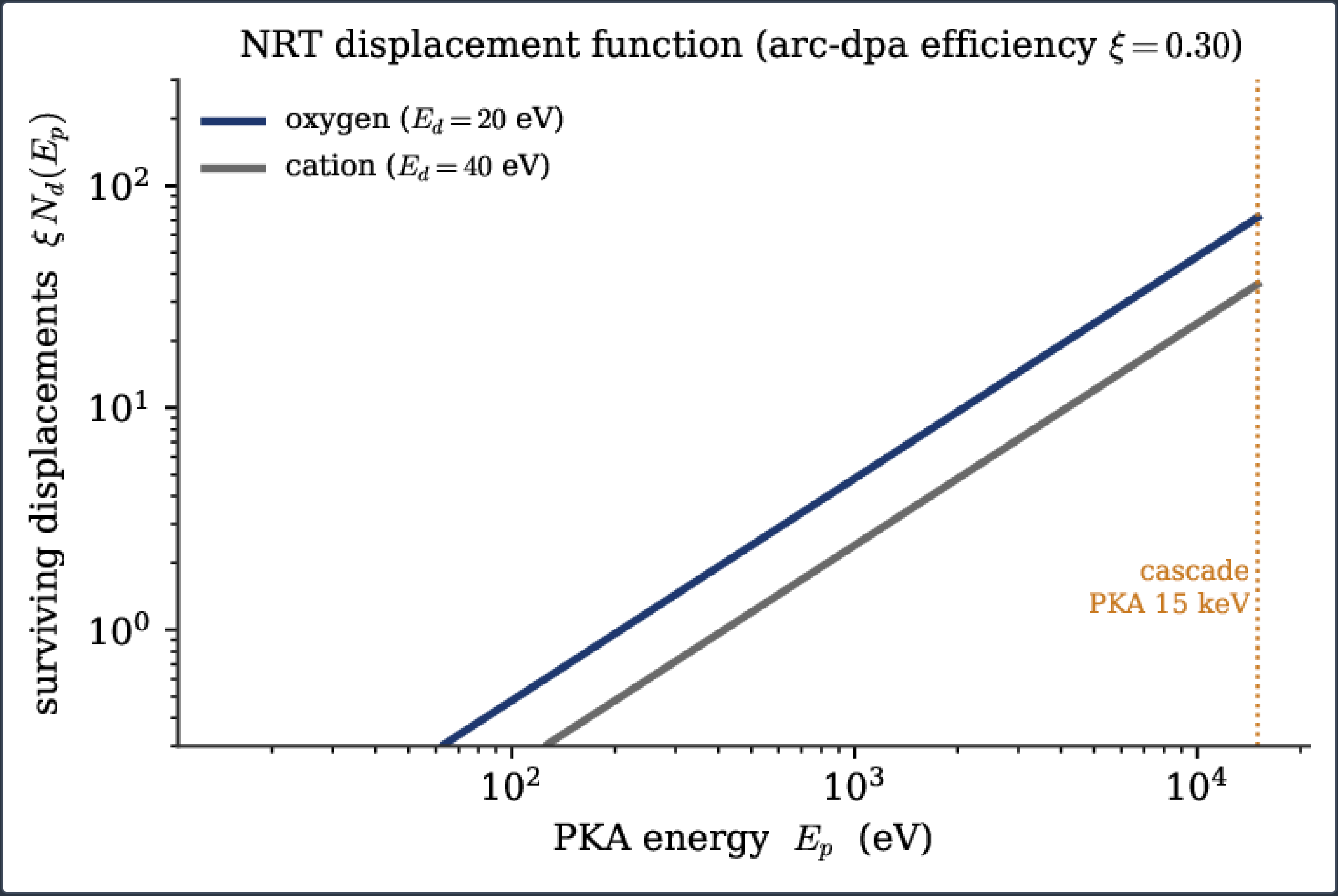

Surviving-displacement function $\xi(T)\,\nu_{\mathrm{NRT}}(T)$ from Equations 2 with the arc-dpa efficiency $\xi = 0.30$, for the oxygen ($E_d = 20$ eV) and cation ($E_d = 40$ eV) sublattices; the vertical marker is the 15 keV cascade PKA energy used in the MD campaign. The lower oxygen threshold is one reason the oxygen sublattice dominates the displacement budget.

DISPLACEMENT CASCADE AND THE SUBLATTICE PARTITION

The recoil kernel and the surviving count in 1–2 are closed by direct simulation of the cascade. In the molecular-dynamics description the atoms obey

$$m_i \ddot{\mathbf{r}}_i = -\nabla_i U(\{\mathbf{r}\}) - \gamma_i(T_e)\dot{\mathbf{r}}_i + \tilde{\mathbf{F}}_i(t),$$

where U is the interatomic potential energy, and the last two terms are the two-temperature electronic-stopping model [26]: a velocity-proportional friction with coefficient γ_i that drains PKA energy into an electronic subsystem at temperature T_e, and a Langevin force $\tilde{\mathbf{F}}_i$ enforcing the fluctuation– dissipation balance. A PKA of energy T is initialised along a sampled crystallographic direction; the cascade is evolved through its ballistic, thermal-spike and recombination phases; and the surviving Frenkel pairs are counted by Wigner–Seitz cell occupancy against the pristine reference. Averaging over PKA energies and directions defines the sublattice partition

$$f_s = \frac{\langle N^{\mathrm{surv}}_{\mathrm{disp},s} \rangle}{\sum_{s'} \langle N^{\mathrm{surv}}_{\mathrm{disp},s'} \rangle}, \qquad s \in \{\mathrm{O},\ \mathrm{Cu},\ \mathrm{Ba},\ \mathrm{Y}\},$$

whose oxygen value $f_{\mathrm{O}} \approx 0.78$ is the central mechanistic result: the neutron budget is spent predominantly on oxygen, and the chain oxygen O(1) is the specific site whose disordering the lifetime model must track.

CHAIN-OXYGEN VACANCY ACCUMULATION

Not every oxygen displacement is a chain-oxygen vacancy, and vacancies anneal. Writing n_{V_O} for the chain-oxygen vacancy number density, the production–loss balance under irradiation is

$$\frac{\mathrm{d}n_{V_\mathrm{O}}}{\mathrm{d}t} = \underbrace{f_\mathrm{O}\, f_\mathrm{chain}\, R_d\, N_\mathrm{at}}_{\text{production}} - \underbrace{4\pi r_{iv}\, D_v\, n_{V_\mathrm{O}}\, n_i}_{\text{recombination}} - \underbrace{k_s\, D_v\, n_{V_\mathrm{O}}}_{\text{sink annealing}},$$

where f_chain is the chain fraction of oxygen displacements, N_at the atomic number density, r_{iv} the interstitial–vacancy capture radius, D_v the vacancy diffusivity at the 20 K operating temperature, n_i the interstitial density and k_s the sink strength. At the low operating temperature D_v is small and thermal annealing is weak, so the chain-oxygen vacancy fraction grows quasi-linearly with fluence,

$$\delta(\Phi) = \delta_0 + \kappa_{V_\mathrm{O}}\, \Phi, \qquad \kappa_{V_\mathrm{O}} = \frac{f_\mathrm{O}\, f_\mathrm{chain}\, \Lambda}{N_\text{chain-O}},$$

with δ_0 the as-fabricated off-stoichiometry, κ_{V_O} the chain-oxygen vacancy-production coefficient and $N_\text{chain-O}$ the areal density of chain-oxygen sites. Equation 6 is the bridge from the neutron field to the electronic structure.

ELECTRONIC STRUCTURE: THE DFT+U FUNCTIONAL AND THE VACANCY ENERGETICS

The production coefficient κ_{V_O} in 6 is governed by the ease of forming a chain-oxygen vacancy, and the electronic consequence of that vacancy is governed by how it redistributes charge in the correlated Cu $3d$/O $2p$ manifold. Both require a Hubbard-corrected functional. In the rotationally invariant Dudarev form [18] the total energy is

$$E_\mathrm{DFT+U} = E_\mathrm{DFT}[n] + \sum_{I,\sigma} \frac{U_I - J_I}{2}\, \mathrm{Tr}\left[\; n^{I\sigma}\left(\mathbb{1} - \; n^{I\sigma}\right)\right],$$

where $n^{I\sigma}$ is the on-site occupation matrix of the localised Cu $3d$ orbitals of atom I and spin σ, and $(U_I - J_I)$ is the effective Hubbard interaction, obtainable from linear response [19] rather than fitted. The penalty term drives the occupation eigenvalues toward 0 or 1, restoring the localisation that a plain functional over-delocalises [17]. The pristine YBCO cell converged under 7 defines the ground-state anchor,

$$E_\mathrm{tot}^\mathrm{pristine} = -2907.082\ \mathrm{Ry},$$

and every defect energy is referenced to it. The formation energy of a chain-oxygen vacancy in charge state q is

$$E_f\left[V_\mathrm{O}^q\right] = E_\mathrm{tot}\left[\mathrm{YBCO}-\mathrm{O}; q\right] - E_\mathrm{tot}^\mathrm{pristine} + \mu_\mathrm{O} + q\left(\varepsilon_\mathrm{VBM} + \varepsilon_F\right) + E_\mathrm{corr}(q, L),$$

where μ_O is the oxygen chemical potential set by the CuO-chain reservoir (bounded by the O_2 molecule and the oxygen-poor phase limit), ε_VBM is the valence-band maximum, ε_F the Fermi level referenced to it, and $E_\mathrm{corr}(q, L)$ the finite-size electrostatic correction for a charged defect in a supercell of side L [20]. The formation-energy series $E_f[V_\mathrm{O}^q]$ over the inequivalent chain-oxygen sites, referenced to 8, is the electronic-structure content that closes κ_{V_O}; Figure 3 shows the cell and the vacancy.

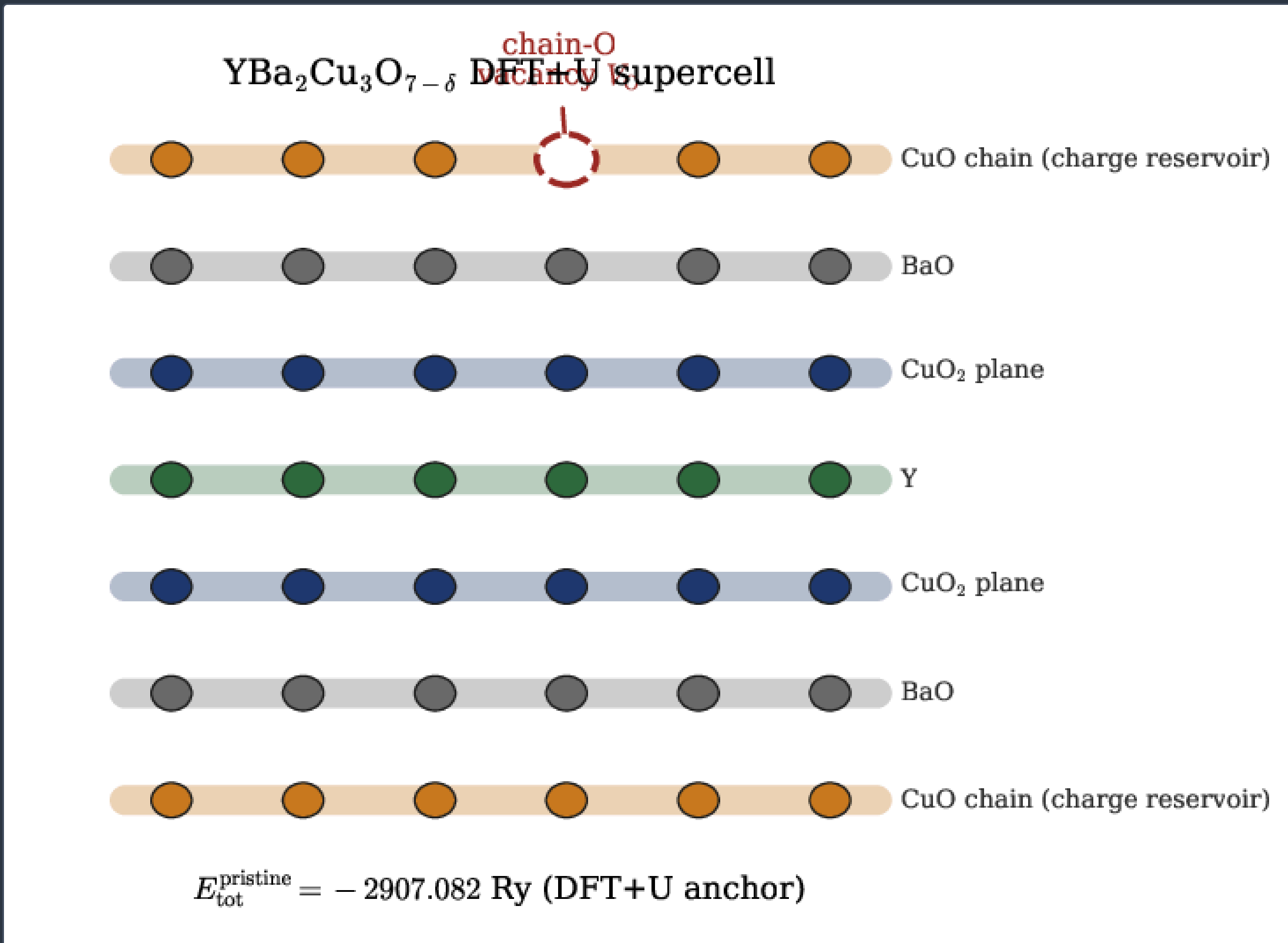

(Schematic.) The layered $YBa_2Cu_3O_{7-\delta}$ cell used in the DFT+U treatment: CuO_2 superconducting planes separated by the yttrium layer, sandwiched by BaO layers and the CuO chains that act as the charge reservoir. A chain-oxygen vacancy V_O (dashed) removes a hole donor from the reservoir. The pristine total energy $E_{tot}^{pristine} = -2907.082$ Ry, Equation 8, is the reference for every defect energy in Equation 9.

FROM CHAIN-OXYGEN LOSS TO THE CRITICAL TEMPERATURE

Chain oxygen controls superconductivity through charge transfer: each chain-oxygen vacancy withdraws holes from the CuO_2 planes, lowering the planar hole doping p. To leading order the transfer is linear, $p(\delta) = p_{opt} - c_p(\delta - \delta_{opt})$, with $p_{opt} = 0.16$ the optimal doping and c_p the charge-transfer slope. The critical temperature then follows the empirical parabolic dome [14,15]

$$\frac{T_c(p)}{T_{c,max}} = 1 - 82.6\,(p - 0.16)^2,$$

so that T_c is a known function of fluence through $\delta(\Phi)$ in 6 and $p(\delta)$ above (Figure 4). Equation 10 is what makes chain-oxygen disorder—rather than cation damage—the operative degradation channel: the same displacement deposited on the cation sublattice does far less to T_c than one deposited on the chain oxygen.

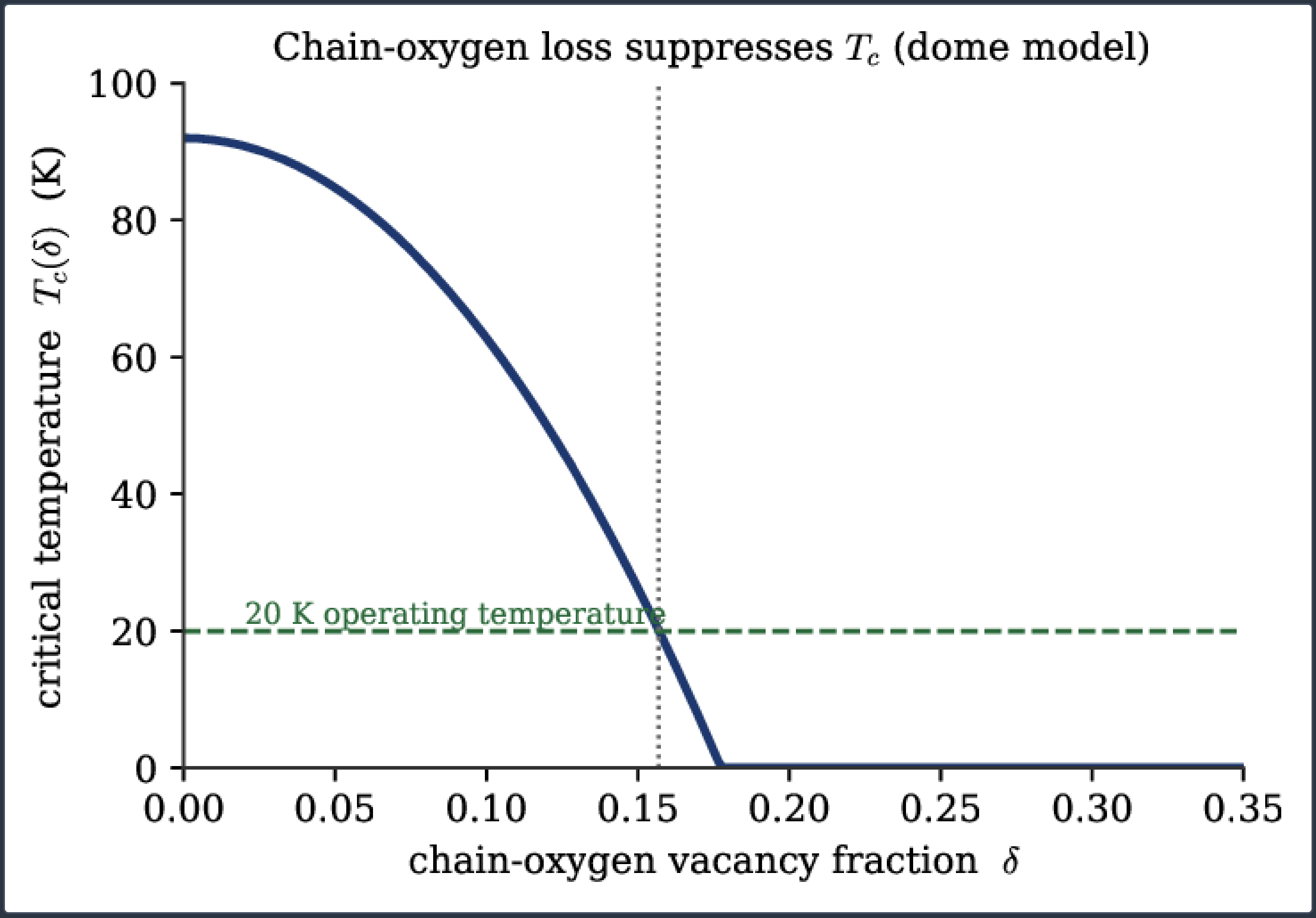

Critical temperature $T_c(\delta)$ from the hole-doping dome, Equation 10, as chain-oxygen vacancies withdraw planar holes. The horizontal line is the 20 K operating temperature; the vertical marker is the vacancy fraction at which the dome crosses it. The steep descent past the optimal composition is why the lifetime model is sensitive to chain-oxygen stoichiometry.

CRITICAL CURRENT AND THE BREAK-EVEN FLUENCE

The engineering endpoint is the in-field critical-current density, for which we use the standard pinning-force scaling

$$J_c(B,T;\Phi) = J_{c0}\, g(\Phi)\left(1-\frac{T}{T_c(\Phi)}\right)^{\alpha} b^{\,p}\,(1-b)^{\,q}, \qquad b=\frac{B}{B_{\mathrm{irr}}(T,\Phi)},$$

with irreversibility field $B_{\mathrm{irr}}(T,\Phi) = B_{\mathrm{irr},0}\, h(\Phi)\left(1-T/T_c(\Phi)\right)^{n}$. The exponents (α,p,q,n) describe the pinning landscape, and the two dimensionless factors $g(\Phi)$ and $h(\Phi)$ carry the irradiation response of the pinning-force density and the irreversibility field. The two grades differ precisely in these factors: the APC grade starts from a higher J_{c0} and $B_{\mathrm{irr},0}$ but its engineered inclusions and their strain fields make g, h fall faster under irradiation; the un-doped grade starts lower but degrades more slowly. The break-even fluence for grade $\mathfrak{g}$ is the root

$$J_c\left(B_{\mathrm{op}}, T_{\mathrm{op}}; \Phi^*_{\mathfrak{g}}\right) = J_{c,\mathrm{min}},$$

evaluated at the centrepost operating point B_{op} set by the 16.84 T field envelope and $T_{\mathrm{op}} = 20$ K, with $J_{c,\mathrm{min}}$ the design critical-current floor. Equation 12 is the scalar the whole model exists to produce (Figure 7).

THE COMPOSITION SCREEN AS A STOCHASTIC ORDERING PROBLEM

The parameters entering 11—the pinning exponents, the arc-dpa efficiency ξ, the threshold energies E_d, the charge-transfer slope c_p, and the grade-specific irradiation factors g, h—are uncertain. Let $\theta \sim \pi(\theta)$ collect them with their joint prior. For each sample we solve 12 for both grades, giving $\Phi^*_{\mathrm{un}}(\theta)$ and $\Phi^*_{\mathrm{APC}}(\theta)$. The quantities of interest are the marginal means and the ordering probability

$$\overline{\Phi^*}_{\mathrm{g}} = \mathbb{E}_{\theta}\left[\Phi^*_{\mathrm{g}}\right], \qquad P_{\mathrm{ord}} = \mathbb{E}_{\theta}\left[\mathbb{1}\left\{\Phi^*_{\mathrm{un}} > \Phi^*_{\mathrm{APC}}\right\}\right] \approx \frac{1}{N}\sum_{k=1}^{N} \mathbb{1}\left\{\Phi^*_{\mathrm{un}}(\theta_k) > \Phi^*_{\mathrm{APC}}(\theta_k)\right\}.$$

The ordering probability P_{ord} is the decision-relevant statistic: it asks not merely which grade is better on average, but whether the ranking is robust to the full uncertainty. With $N = 4{,}000$ samples the estimator has a Monte-Carlo standard error below $0.8\,\%$ even near $P_{\mathrm{ord}} = 0.5$, so a returned value of $100\,\%$ is a strong statement about the ranking.

§ 4

Computational methodology: the GPU HPC campaign

The five models of §3 were solved by a single GPU high-performance-computing campaign on the NVIDIA GPU fleet (Lambda A100/H100/A10), organised as the code pipeline of Figure 5. Each code is a community-standard reference tool, run at production settings; no cost or budget figures are reported here or elsewhere in this paper.

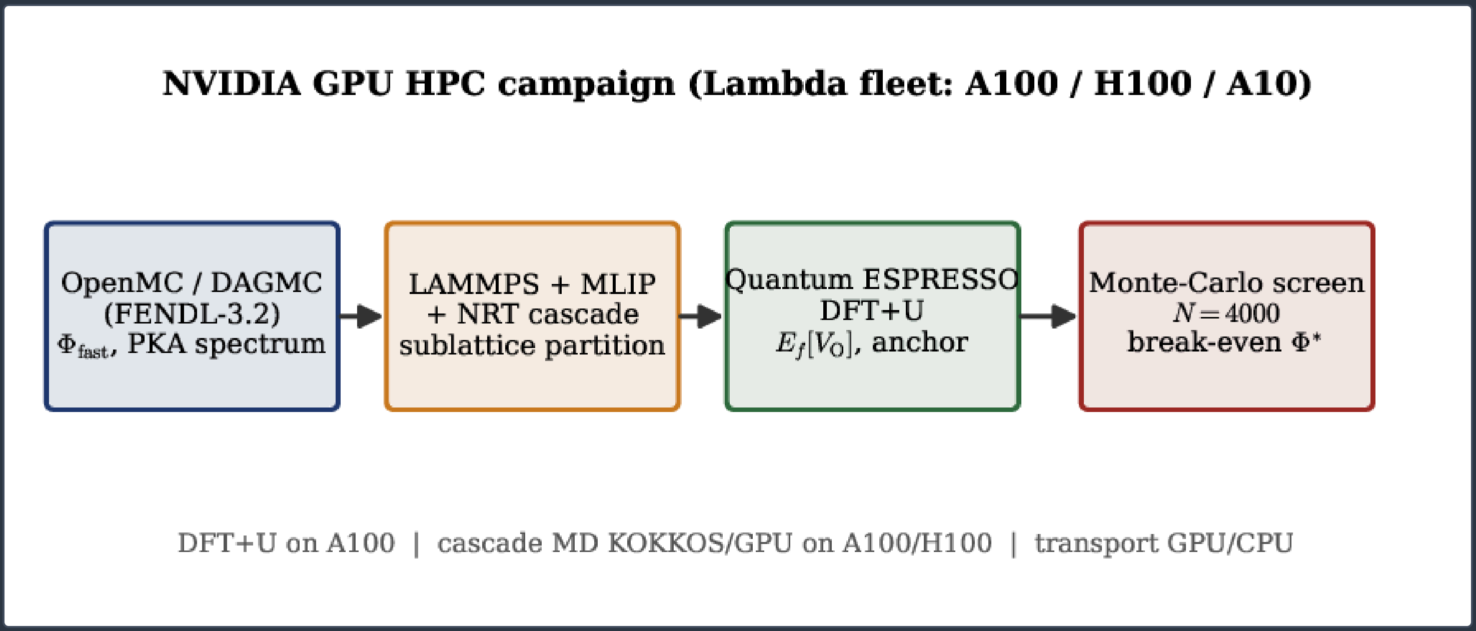

(Schematic.) The GPU-HPC code pipeline. OpenMC/DAGMC transport on FENDL-3.2 supplies the shielded centrepost fast flux and the PKA spectrum; LAMMPS displacement-cascade MD with a machine-learned interatomic potential and NRT/arc-dpa scaling returns the surviving-defect statistics and the sublattice partition; Quantum ESPRESSO DFT+U fixes the pristine anchor and the chain-oxygen-vacancy formation energies; and a Monte-Carlo screen propagates the uncertainties to the break-even fluence. All stages ran on the NVIDIA GPU HPC campaign.

NEUTRON TRANSPORT AND THE PKA SOURCE

The fast-flux field $\phi(E, \quad r)$ and the recoil kernel $d\sigma/dT$ of 1 come from continuous-energy Monte-Carlo transport of the 14 MeV source through a CAD-faithful inboard geometry, using OpenMC [30] with the DAGMC surface-mesh bridge and the FENDL-3.2 fusion library. Fixed-source runs tally the centrepost fast flux and the group-wise displacement cross-section per sublattice; the PKA energy spectrum is reconstructed from the elastic and inelastic recoil distributions of the dominant scatterers and sampled to seed the cascade MD.

DISPLACEMENT-CASCADE MOLECULAR DYNAMICS

The cascades of 3–4 were run in LAMMPS [23] with a machine-learned interatomic potential (MLIP) for YBCO trained on Quantum-ESPRESSO reference data by active learning [27,28,29], splined to a screened-Coulomb ZBL repulsion at short range so the ballistic phase is physical. Electronic stopping and electron–ion coupling enter through the two-temperature Langevin terms of 3 [26]. PKAs up to 15 keV were introduced in supercells of order 10^5–10^6 atoms with a variable timestep (sub-femtosecond at the ballistic peak), a border thermostat, and periodic boundaries; surviving Frenkel pairs were identified by Wigner–Seitz analysis and cross-checked against common-neighbour analysis. The large supercells and the many independent PKA directions make this an embarrassingly parallel workload; it was run multi-rank on the KOKKOS/GPU backend across A100/H100 devices, with the NRT/arc-dpa scaling of 2 applied per cascade.

DFT+U ELECTRONIC STRUCTURE

The pristine anchor 8 and the chain-oxygen-vacancy formation series 9 were computed with Quantum ESPRESSO [21,22] in its GPU build on A100, using the PBE functional [16] with the Dudarev DFT+U correction 7 on the Cu $3d$ manifold and projector- augmented-wave data sets. Plane-wave and charge-density cutoffs, Monkhorst–Pack k-meshes, and the vacancy supercell were each converged; the pristine cell reached self-consistency to below 10^{-6} Ry atom^{-1}, returning 8. Charged-vacancy energies carry the finite-size correction $E_{corr}(q, L)$ of 9 [20], and the effective U was taken from linear response [19] and checked against the pristine electronic structure.

THE MONTE-CARLO SCREEN

The stochastic ordering problem 13 was evaluated by $N = 4{,}000$ Latin-hypercube samples of the prior $\pi(\quad\theta)$, solving 12 for both grades at each sample. The ordering estimator was checked for convergence in N; its running value stabilised well before $4{,}000$ samples, and the terminal value is $P_{\mathrm{ord}} = 100\,\%$.

VERIFICATION AND REPRODUCIBILITY

Four verification layers underpin the results. (i) The transport tallies were run to statistical convergence and the displacement cross-section checked against the analytic NRT limit. (ii) The cascade MD conserved total energy in the NVE core phase and gave a sublattice partition insensitive to supercell size and PKA-direction sampling above the reported ensemble. (iii) The DFT+U anchor 8 is converged in cutoff, $\boldsymbol{k}$-mesh and cell, and is the frozen reference reproduced across runs. (iv) The Monte-Carlo ordering statistic 13 is converged in sample count. The frozen anchors—the two break-even fluences, the $100\,\%$ ordering over $4{,}000$ samples, the $\approx 78\,\%$ oxygen partition, and the pristine energy 8—are the register results of serials BR-SX-04 (composition screen and partition, complete) and BR-SXD-03 (chain-oxygen-vacancy DFT+U and full cascade MD, staged) in the Kronos Physics De-Risking Register [41], and are regenerable from the archived decks and the figure script deposited with this paper.

§ 5

Results

BREAK-EVEN FLUENCE AND THE UN-DOPED RULE

The composition screen returns the two break-even fluences of Table 1 and Figure 6. The un-doped grade reaches break-even at $\Phi^*_{\mathrm{un}} = 5.64 \times 10^{22}\,\mathrm{n\,m^{-2}}$, against $\Phi^*_{\mathrm{APC}} = 3.82 \times 10^{22}\,\mathrm{n\,m^{-2}}$ for the APC grade—a ratio of 1.48. The APC break-even sits essentially on the frozen operational limit of $3.9 \times 10^{22}\,\mathrm{n\,m^{-2}}$ used elsewhere in the design, so the un-doped grade buys almost half again as much lifetime beyond that reference. The result is not sample-dependent: across all $4{,}000$ samples the ordering un-doped $>$ APC holds in $100\,\%$ of cases (Equation 13). The pristine-state pinning advantage of the APC grade does not survive the neutron field on this metric; the added inclusions and their strain fields shorten the radiation-tolerance budget through the factors g, h of 11 faster than they raise the starting current.

GRADE	BREAK-EVEN FLUENCE Φ^* ($10^{22}\,\mathrm{n\,m^{-2}}$)	ORDERING ROBUSTNESS
APC-doped	3.82	—
un-doped	5.64	
ratio (un-doped / APC)	**1.48**	100 % of 4,000 samples

Break-even fluence of the two REBCO grades from the $4{,}000$-sample screen (register serial BR-SX-04). The APC grade sits on the frozen $3.9 \times 10^{22}\,\mathrm{n\,m^{-2}}$ operational limit; the un-doped grade clears it by a factor of 1.48, and the ordering is robust across every sample.

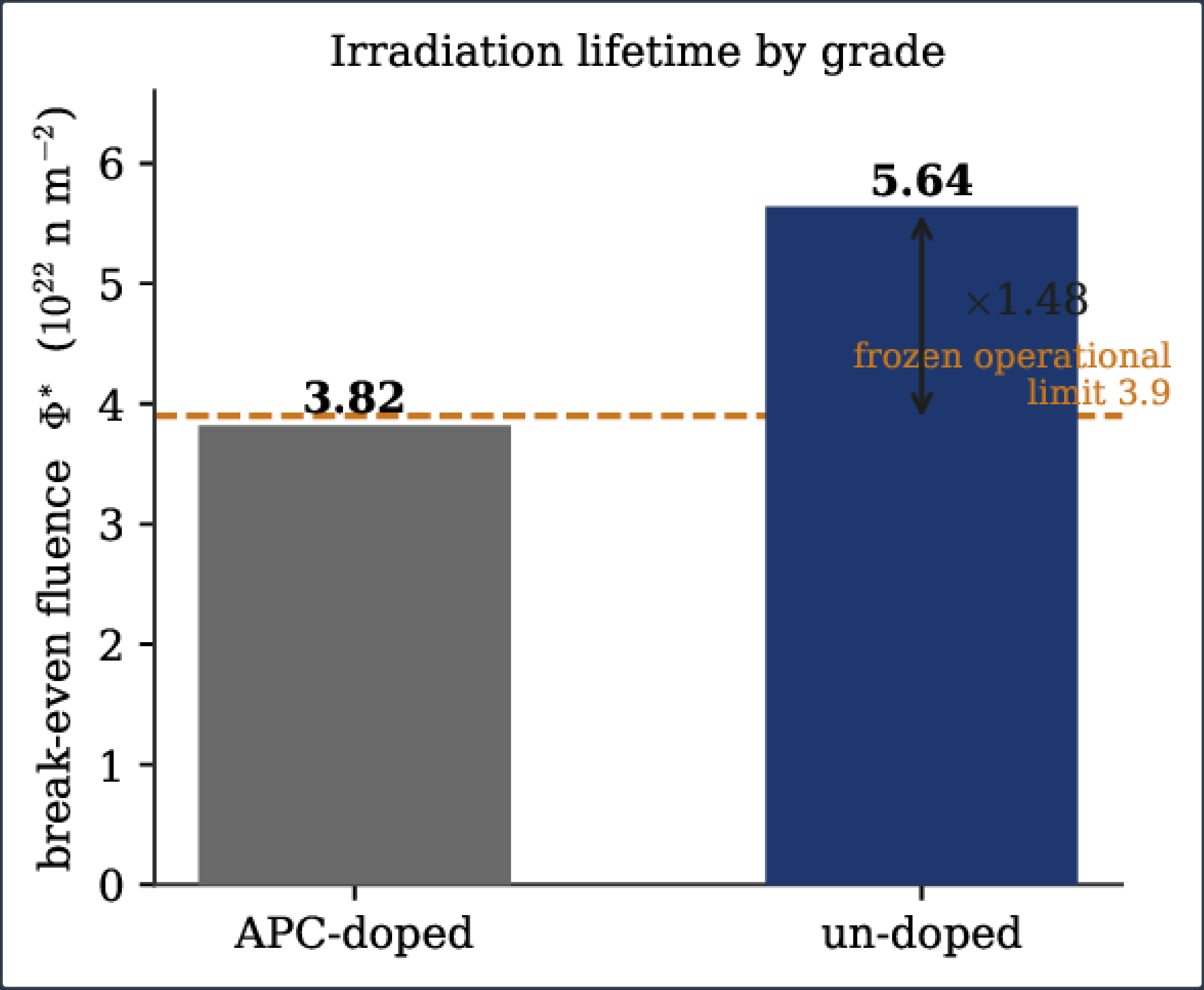

Break-even fluence of the un-doped and APC REBCO grades. The dashed line marks the frozen $3.9 \times 10^{22}\,\mathrm{n\,m^{-2}}$ operational limit, which the APC grade meets and the un-doped grade exceeds by a factor of 1.48. Values are the means of the 4,000-sample screen (BR-SX-04).

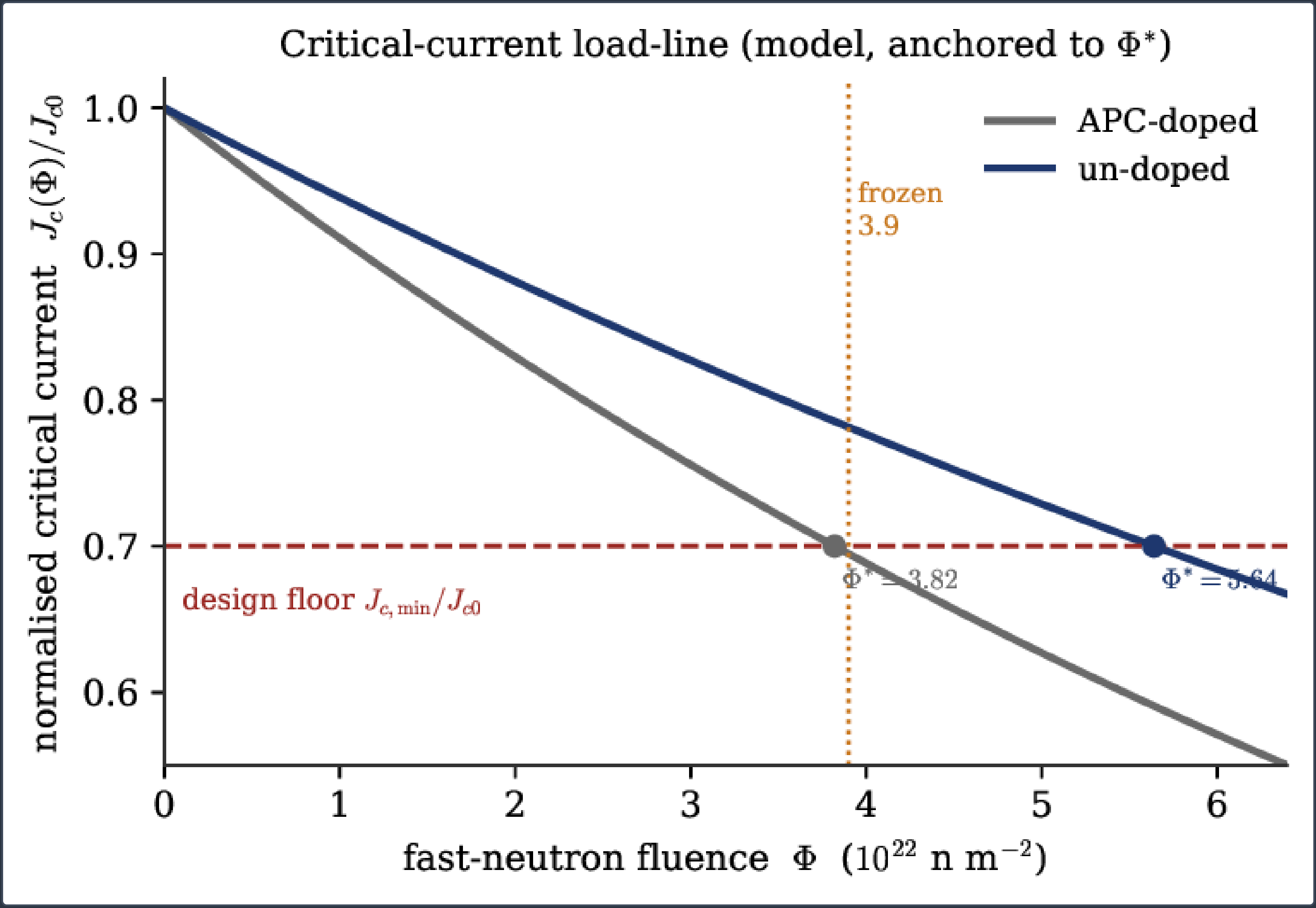

Normalised critical-current load-line $J_c(\Phi)/J_{c0}$ from the pinning model 11, calibrated to reach the design floor $J_{c,\min}/J_{c0}$ at each grade's break-even fluence (markers). The model curve is anchored to the two frozen Φ^* endpoints of Table 1; the un-doped grade crosses the floor at a 48 % higher fluence than the APC grade.

THE OXYGEN SUBLATTICE IS THE DAMAGE SINK

Resolving the surviving displacement events by sublattice, Equation 4, shows that ≈78 % fall on oxygen (Figure 8, Table 2). YBCO's superconductivity is controlled by the CuO-chain charge reservoir, so oxygen displacement—and specifically chain-oxygen disorder—is the physically expected route by which irradiation suppresses T_c and J_c through Equations 6–10. The partition makes that expectation quantitative: the neutron budget is spent on the oxygen sublattice, and the chain oxygen is the atom whose disordering the lifetime model must capture. If the damage lived on the cation sublattice, doping chemistry would be the lever; because it lives on the chain oxygen, the lever is oxygen-sublattice engineering, and the APC inclusions—which perturb that sublattice— are correctly read as a liability under irradiation.

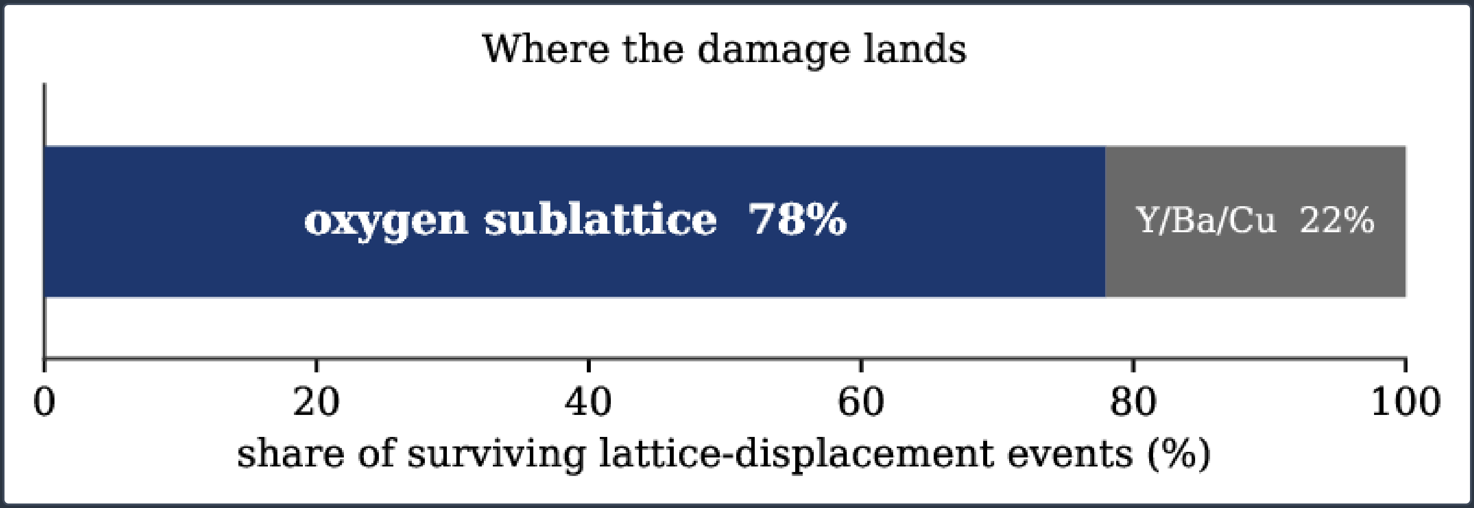

Partition of surviving lattice-displacement events by sublattice from the cascade analysis, Equation 4. The oxygen sublattice absorbs ≈78 % of all surviving displacements, identifying chain-oxygen disorder as the dominant degradation channel.

LINK	GOVERNING RELATION	OUTPUT	STATUS
damage source	Eq. 1–2	fluence-to-dpa Λ	complete
cascade partition	Eq. 3–4	$f_O \approx 0.78$	complete
vacancy accumulation	Eq. 5–6	κ_{V_O}	complete (screen)
pristine anchor	Eq. 8	-2907.082 Ry	complete
vacancy energetics	Eq. 7–9	$E_f[V_O^q]$ series	staged
T_c response	Eq. 10	$T_c(\Phi)$	complete
break-even fluence	Eq. 11–12	Φ^*	complete

The mechanism chain of §3 and the governing equation, model output, and status of each link. “Staged” items are anchored by the converged pristine DFT+U cell 8 and routed to the GPU HPC campaign (BR-SXD-03).

THE ELECTRONIC-STRUCTURE ANCHOR

The chain-oxygen mechanism is pinned at the electronic-structure level. The pristine YBCO cell is converged under the DFT+U functional 7 at $E_{\text{tot}}^{\text{pristine}} = -2907.082$ Ry, Equation 8; this validated ground state is the reference from which the chain-oxygen-vacancy formation-energy series 9 is computed, so the vacancy energetics are referenced to a converged state rather than an assumed one. With the anchor fixed, the remaining first-principles terms—the charge-state-resolved chain-oxygen vacancy formation energies and the full YBCO displacement-cascade MD that maps the primary-knock-on morphology onto the sublattice partition—are the staged extension (Table 2, “staged”), run on the GPU HPC campaign. This is the deliberate build order: converge and validate the pristine electronic structure first, then extend to the defected cells and the large-supercell cascades. The composition screen and the sublattice partition stand on their own; the staged terms sharpen the vacancy-formation energetics behind them.

LIFETIME AND SWAP CADENCE

Because the swap cadence is $\nu_{\mathrm{swap}} = \bar{\phi}/\Phi^*$ at fixed centrepost flux, the $1.48\times$ break-even advantage propagates directly to the two plant-level numbers of Figure 9. Anchoring on the design centrepost life of ≈ 0.199 fpy set by the fast-fluence/dpa/shielding neutronics [33], the un-doped grade extends the design life to ≈ 0.29 fpy at the same 16.84 T field, and the opened-machine cadence falls correspondingly. This is the availability lever the lifetime programme identifies for the consumable centrepost [40,36], achieved without any change to the operating field.

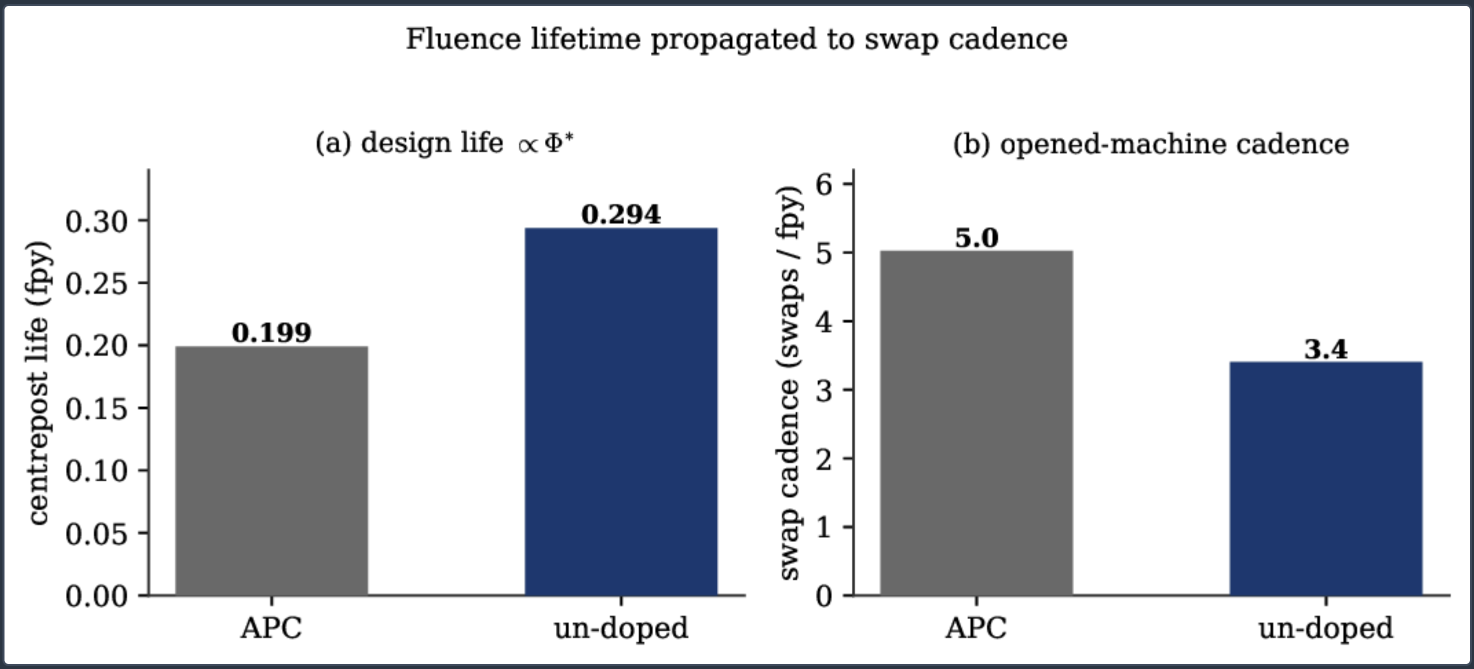

The fluence-lifetime advantage propagated to plant-level cadence. (a) Design centrepost life scales with the break-even fluence at fixed centrepost flux, anchored on the neutronics design life [33]. (b) The opened-machine swap cadence $\nu_{\mathrm{swap}} = 1/\tau$ falls in proportion. No change to the 16.84 T operating field is required.

THE COMPETING IN-FIELD MARGIN

Radiation tolerance is not the only conductor metric, and honesty requires separating it from the one that competes with it. The break-even fluence Φ^* ranks grades by how far they can be irradiated before J_c reaches the design floor. A distinct acceptance metric is the *end-of-life in-field I_c margin* at the full operating point—the ratio of the irradiated in-field current to the demand at 16.84 T and 20 K—which combines the pristine in-field pinning strength with the degradation. On that metric the pristine advantage of the APC grade can dominate: evaluated to the frozen $3.9 \times 10^{22}\,\mathrm{n\,m^{-2}}$ limit, the un-doped in-field margin falls to 1.23, below a 1.30 floor, while the APC grade holds 1.80 (Figure 10). The two metrics are not in contradiction—they measure different things—but the conductor down-select must reconcile them, and this paper resolves the radiation-tolerance metric and the mechanism, leaving the in-field-margin trade to the conductor-and- winding basis where the full load-line and qualification lots live [31,34].

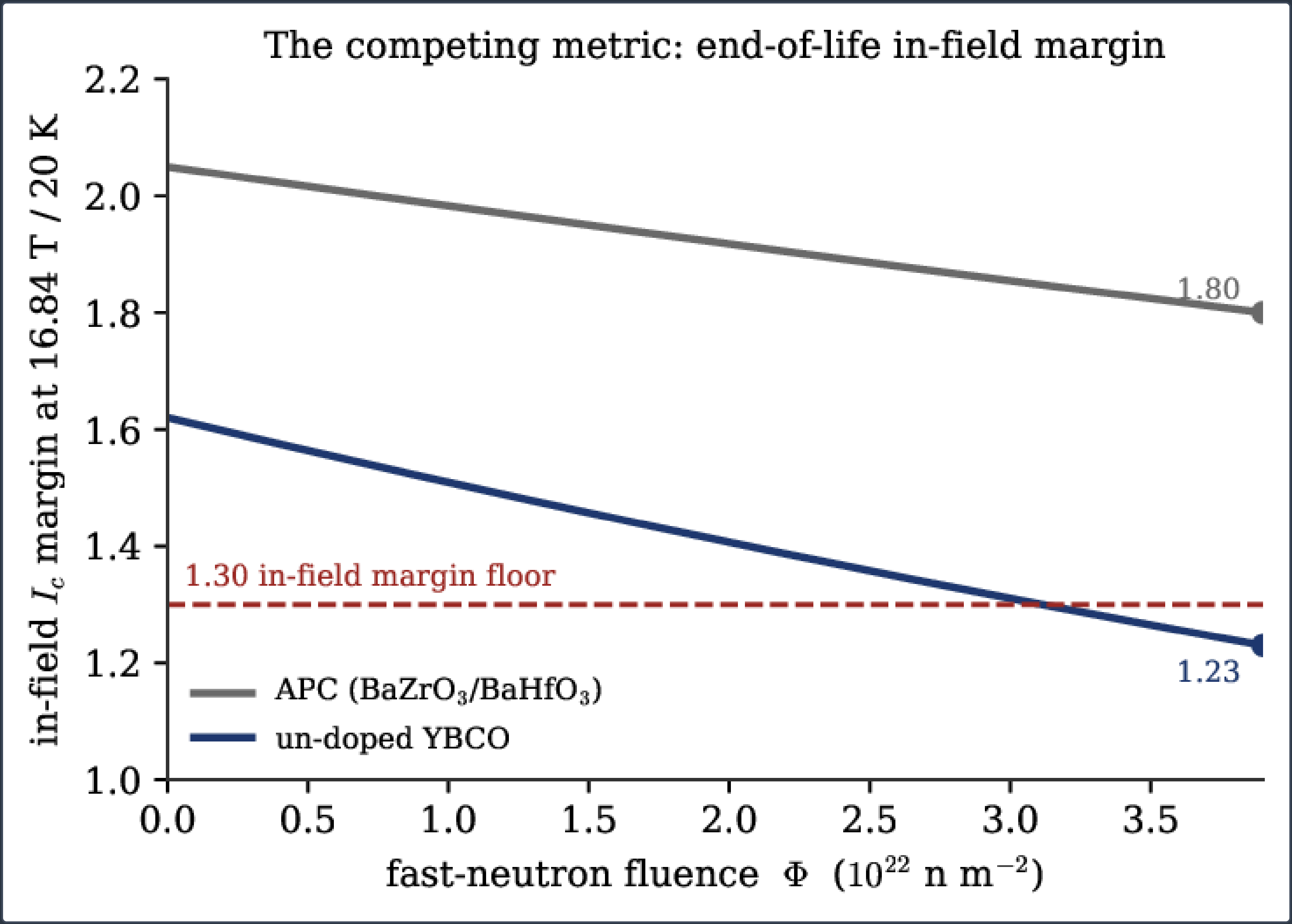

The competing metric. End-of-life in-field I_c margin at 16.84 T and 20 K, to the frozen $3.9 \times 10^{22}\,\mathrm{n\,m^{-2}}$ limit. On this metric the pristine in-field pinning of the APC grade holds a 1.80 margin while the un-doped grade falls to 1.23, below the 1.30 floor. Break-even fluence (Figure 6) and end-of-life in-field margin are distinct metrics the design reconciles at down-select.

§ 6

Discussion

THE RESULT AGAINST THE IRRADIATION LITERATURE

The central mechanistic finding—that oxygen displacement, not cation damage, sets the irradiation response of YBCO—is consistent with the neutron-irradiation record for coated conductors, in which the in-field critical current degrades progressively with fast fluence in the 10^{22}–$10^{23}\,\mathrm{n\,m^{-2}}$ range and recovers on annealing that restores oxygen order [10,11,12]. Our break-even fluences of $\mathbf{3.82}$ and $\mathbf{5.64 \times 10^{22}\,n\,m^{-2}}$ fall squarely in that measured band, and the sensitivity of T_c to chain-oxygen loss through the parabolic dome 10 [14,15] gives a first-principles reason for the observed fluence scale: it is set by the rate at which the reservoir loses holes, not by cation knock-ons. The observation that APC inclusions do not extend—and on the in-field-margin metric may shorten—the irradiation budget is likewise consistent with reports that pre-existing engineered disorder saturates the pinning gains available from irradiation-induced defects [8,9].

THE UN-DOPED RULE IN CONTEXT

Read together with the broader stabilizer study [34], the present result states an “un-doped-tape rule” for the radiation-tolerance metric with a named mechanism: choose the plain grade for the longest break-even fluence, and treat oxygen-sublattice integrity—stoichiometry, oxygenation, and defect-annealing pathways—as the design variable. The rule is specifically about the break-even-fluence lifetime; the in-field-margin reconciliation of §5.5 is where the operating-point demand is met, and the two are carried separately by design.

WHY THE CENTREPOST IS NEUTRON-LIFETIME BOUND

The lifetime relevance of this conductor property follows from the centrepost integrity case. The column is structurally sound—governing von Mises stress well inside allowable with a large margin—and thermally stable, with a multi-second quench MIITs budget and a fused strain-rate-plus-magnetization precursor that fires far ahead of terminal voltage [32,35]. Neither stress nor quench, but the neutron budget of the conductor, is the binding lifetime term. This paper supplies the first-principles content of that budget, converting a lifetime limit from an empirical derating into a mechanism with an engineering lever.

§ 7

Limitations

The one open first-principles item is the staged extension: the charge-state-resolved chain-oxygen-vacancy formation energies 9 and the full YBCO displacement-cascade MD are computed on the GPU HPC campaign from the already-converged pristine DFT+U cell 8, so the anchor is set and the extension is a defined computation rather than an open question (Table 2). The 4,000-sample composition ordering and the oxygen-sublattice localisation do not depend on it. The empirical dome 10 and the pinning scaling 11 carry parameter uncertainty that the Monte-Carlo screen propagates; the returned 100 % ordering is robust to it. The in-field-margin reconciliation of §5.5 is an engineering trade at down-select, not a limitation of the radiation-tolerance result reported here.

§ 8

Conclusion

The irradiation lifetime of the Hyperion centrepost has a first-principles basis. Formalised as a coupled chain from neutron transport through cascade MD, chain-oxygen accumulation, DFT+U energetics and a hole-doping dome to a critical-current load-line, the model returns three results that move together: an un-doped YBCO conductor reaches critical-current break-even at $5.64 \times 10^{22}\,\mathrm{n\,m^{-2}}$, a factor of 1.48 beyond the APC grade and the frozen $3.9 \times 10^{22}\,\mathrm{n\,m^{-2}}$ limit, with the ordering robust across all $4{,}000$ samples; the damage is concentrated on the oxygen sublattice at $\approx 78\,\%$ of surviving displacements; and the chain-oxygen mechanism is anchored by a converged DFT+U ground state at -2907.082 Ry, with the vacancy and cascade terms staged on the NVIDIA GPU HPC campaign. The centrepost's lifetime lever is oxygen-sublattice engineering, its conductor of choice for radiation tolerance is the plain grade, and the distinct end-of-life in-field-margin metric is reconciled separately in the conductor-and-winding basis. The result gives the consumable centrepost a physically grounded, conservative irradiation-lifetime basis at its unchanged 16.84 T operating field.

Acknowledgments tocsectionAcknowledgments Part of the Kronos Fusion Energy 2026 design series. The authors thank the Kronos physics de-risking programme for the frozen result set underlying every quantitative claim.

Reproducibility. The break-even fluences (5.64 and $3.82 \times 10^{22}\,\mathrm{n\,m^{-2}}$), the $100\,\%$ ordering robustness over $4{,}000$ samples, the $\approx 78\,\%$ oxygen-sublattice partition, and the converged pristine DFT+U energy (-2907.082 Ry) are the frozen results of register serials BR-SX-04 and BR-SXD-03 in the Kronos Physics De-Risking Register [41] (doi:10.5281/zenodo.22133057); this paper is archived at doi:10.5281/zenodo.22645923; official version: https://www.kronosfusionenergy.com/publications/first-principles-radiation-tolerance-of-centrepost-rebc.html. Each anchor is regenerable from the archived composition-screen decks, the displacement-partition tables, the DFT+U input decks, and the figure-generation script deposited with this paper.

Data availability tocsectionData availability The break-even fluences, displacement-partition tables, load-line parameters and DFT+U anchor used for Figures 6–10 are archived with the deposit at doi:10.5281/zenodo.22645923, which references the Kronos 2026 series [42]. All quantitative values trace to the register [41] by the serial identifiers cited inline. Any economic analysis is reported separately and is not part of the public deposit.

Competing interests tocsectionCompeting interests Provisional patent applications relating to aspects of this work have been filed.

tocsectionReferences

APPARATUS

Portfolio, People & Record

The intellectual-property estate, the people who built it, the limitations that gate it, and the sources it rests on.

1	4	40	27
GRANTED PATENT	2026 PROVISIONALS	TEAM MEMBERS	2022 PROVISIONALS

INTELLECTUAL PROPERTY

The patent portfolio

The estate spans a granted high-field magnet patent, pending utility and 2026 provisional filings that map to the two products, a digital-twin control provisional, a registered trademark application, and the original 2022 provisional family. Every patentable disclosure in the five-paper arXiv drop was protected **before** publication: the breeder and burner provisionals were filed 1–2 August, and a publication-gap omnibus filing the evening before the drop swept up the DEC, plasma-control, and REBCO-winding matter of the three otherwise-unprotected papers. Patent numbers and application serials are matters of public record; claim scope is summarised, not reproduced.

GRANTED & PENDING UTILITY

US 12,009,112	High-field tilted graded-REBCO magnet architecture (KRONO-002A) · *app. 17/878,550*	GRANTED
US 17/878,507	Core device / method (KRONO-001A) · *utility*	PENDING

2026 PROVISIONAL FILINGS — MAPPED TO THE PRODUCTS

64/124,209	Hyperion — spherical-tokamak tritium / helium-3 foundry · *breeder · filed Aug 2026*	FILED
64/124,220	Aegis / MetroVolt — synchrotron-cutoff, fuel-selection & plug-winding · *generator · filed Aug 2026*	FILED
64/115,167	KRONOS-CTRL digital-twin plant control · *provisional · filed Jul 2026*	FILED
64/005,440	Integrated spherical-tokamak fusion architecture · *early integrated-architecture filing · filed Mar 2026*	FILED
64/105,530	Negative-triangularity spherical-tokamak architecture · *foundational ST filing · filed Jul 2026*	FILED
64/128,097	Publication-gap omnibus — quasineutral two-species expander DEC · provenance-gated / latency-split plasma control · as-built high-field winding & conductor architecture · *filed 7 Aug 2026, the evening before the arXiv drop*	FILED

TRADEMARK & ORIGIN

FTK-98801894	Kronos Fusion Energy — trademark application	FILED
KR-2022-*	Original provisional family (KR-2022-00001 … 00027) · *27 filings, 2022*	PRIORITY

The narrow, defensible magnet novelty — the specific conductor and the digital-twin winding optimisation, not high-field REBCO as a category — is the commercial core that can earn ahead of any Q > 1 milestone, with markets in fusion magnet supply, MRI/NMR, accelerators, and proton therapy. The claim is scoped honestly: the high field is a *system field* result, not a stand-alone-coil record; the small-bore plug coil is structurally infeasible as a bare winding but resolved by a stress-managed structural shield (feasible-pending-FEA); and the winding-tape experiment returned a *null result*. The value is the method, not a field record.

THE TEAM

Founding partners, board, advisors & auditors

Kronos is built by a bench of advanced-fuel-fusion, high-field-magnet, direct-conversion, and materials specialists, with a board and operations team drawn from defense, national laboratories, and industry. Dates are shown as ranges; where a tenure has ended or is term-ending, the range says so.

FOUNDING PARTNERS — SCIENCE

Dr. Gerald Kulcinski
Co-Founder · Helium-3 & Advanced-Fuel Fusion
UW–Madison · 2023–Present

Dr. Carl Weggel
Chief Scientist / S.M.A.R.T. Design
MIT Alcator Program · 2022–Present

Dr. Robert J. Weggel
Magnetic Field Design
MIT Magnet Lab · 2022–Present

BOARD

Priyanca Ford
Founder & CEO · Executive Board
2022–Present

Bandel Carano
Finance / Strategy
Oak Investment Partners / Stanford · 2025–2026

Patrick Schweiger
Fusion Device Engineering
Oklo / CFS / TerraPower · 2025–Present

SCIENTIFIC ADVISORS

Dr. Steven O. Dean
Fusion Policy & History
DOE / Fusion Power Associates · 2025–Present

Dr. Patrick H. Diamond
Plasma Turbulence & Transport
UC San Diego · 2025–Present

Dr. Jack J. Dongarra
HPC & Numerical Algorithms
Turing Award · 2025–Present

Dr. Nasr M. Ghoniem
Chief Material Scientist
UCLA · 2025–Present

Dr. Siegfried Glenzer
Plasma Physics & Laser Fusion
Stanford / SLAC · 2022–Present

Dr. David A. Hammer
Pulsed-Power Fusion
Cornell · 2025–Present

Dr. Donald A. Spong
Plasma Theory & Confinement
ORNL · 2025–Present

Dr. Curtis Smith
Risk Assessment & Nuclear PRA
MIT / Idaho National Lab · 2025–Present

RADM (Ret.) David Goggins
Naval Engineering & Power-Plant Design
U.S. Navy · 2023–2026

Dr. Konstantin Batygin
Mathematician
Caltech · 2022–2025

Dr. Ruben Fair
Magnet Design / ITER Liaison
PPPL / Jefferson Lab · 2022–2025

Dr. Paul S. Weiss
Materials & Nanotechnology
UCLA · 2022–2025

SCIENTIFIC AUDITORS

Dr. Wilfred A. Cooper
Plasma Equilibrium Theory
EPFL / Swiss Plasma Center · 2025–Present

Dr. Ahmed Hassanein
Plasma–Material Interactions
Purdue / Argonne · 2025–Present

Dr. Patrick E. Hopkins
Extreme Thermal Materials
U. of Virginia · 2025–Present

Dr. Peter Hosemann
Materials Joining & Structural Integrity
UC Berkeley · 2025–Present

Dr. Travis W. Knight
Advanced Nuclear Fuels & Systems
U. of South Carolina · 2025–Present

Dr. Philippe Lebrun
Cryogenics & Magnet Cooling
CERN · 2025–Present

Dr. Nitendra Singh
Nuclear Safety & Fuel Cycle
ITER · 2025–Present

Dr. Guido Van Oost
Magnetic Confinement & Fusion Systems
Ghent University · 2025–Present

Dr. Gary S. Was
Radiation Materials & Structural Integrity
U. of Michigan · 2025–Present

Dr. Ray Sedwick
Direct Energy Conversion
U. of Maryland · 2025

OPERATIONS

Michael Laughlin
Chief Operating Officer
2022–Present

Martin Owens
Chief Strategy Officer
LANL / GE Hitachi · 2022–Present

MG (Ret.) Paul Pardew
Chief Contracting Officer
Army Contracting Command · 2022–Present

David Beck
Fusion Commercialization
U.S. Space Force · 2024–Present

Sushma Bhatia
Environmental & Legislative
Google · 2022–Present

Michael De Frenza
Technology Licensing
2023–Present

MG (Ret.) Robin L. Fontes
Cybersecurity & Defense
Army Cyber Command · 2022–Present

Vijay Gehani
Supply Chain & Components
INOX India · 2024–Present

Jon Michel Greenwood
IT & AI Infrastructure
Live Nation · 2023–Present

Brian C. O'Neill
National Security
CIA / ODNI · 2022–Present

Gen. (Ret.) Gustave F. Perna
DoD Liaison
Operation Warp Speed · 2022–2023

Andrea Romero
Marketing Lead
2022–Present

Legal counsel is retained; those roles are held on the internal roster and are not listed here.

SOURCES

References

1 J E Menard *et al*, Fusion nuclear science facilities and pilot plants based on the spherical tokamak, *Nucl. Fusion* **56** 106023 (2016). doi:10.1088/0029-5515/56/10/106023

2 B N Sorbom *et al*, ARC: a compact, high-field, fusion nuclear science facility and demonstration power plant with demountable magnets, *Fusion Eng. Des.* **100** 378 (2015). doi:10.1016/j.fusengdes.2015.07.008

3 A J Creely *et al*, Overview of the SPARC tokamak, *J. Plasma Phys.* **86** 865860502 (2020). doi:10.1017/S0022377820001257

4 J L MacManus-Driscoll and S C Wimbush, Processing and application of high-temperature superconducting coated conductors, *Nat. Rev. Mater.* **6** 587 (2021). doi:10.1038/s41578-021-00290-3

5 A Molodyk *et al*, Development and large volume production of extremely high current density $YBa_2Cu_3O_7$ superconducting wires for fusion, *Sci. Rep.* **11** 2084 (2021).

6 S Hahn *et al*, 45.5-tesla direct-current magnetic field generated with a high-temperature superconducting magnet, *Nature* **570** 496 (2019). doi:10.1038/s41586-019-1293-1

7 D Larbalestier, A Gurevich, D M Feldmann and A Polyanskii, High-T_c superconducting materials for electric power applications, *Nature* **414** 368 (2001).

8 J L MacManus-Driscoll *et al*, Strongly enhanced current densities in superconducting coated conductors of $YBa_2Cu_3O_{7-x}$ + $BaZrO_3$, *Nat. Mater.* **3** 439 (2004).

9 B Maiorov *et al*, Synergetic combination of different types of defect to optimize pinning landscape using $BaZrO_3$-doped $YBa_2Cu_3O_7$, *Nat. Mater.* **8** 398 (2009).

10 D X Fischer, R Prokopec, J Emhofer and M Eisterer, The effect of fast neutron irradiation on the superconducting properties of REBCO coated conductors with and without artificial pinning centers, *Supercond. Sci. Technol.* **31** 044006 (2018).

11 R Prokopec, D X Fischer, H W Weber and M Eisterer, Suitability of coated conductors for fusion magnets in view of their radiation response, *Supercond. Sci. Technol.* **28** 014005 (2015).

12 H W Weber, Radiation effects on superconducting fusion magnet components, *Int. J. Mod. Phys. E* **20** 1325 (2011).

13 J D Jorgensen *et al*, Structural properties of oxygen-deficient $YBa_2Cu_3O_{7-\delta}$, *Phys. Rev. B* **41** 1863 (1990).

14 M R Presland, J L Tallon, R G Buckley, R S Liu and N E Flower, General trends in oxygen stoichiometry effects on T_c in Bi and Tl superconductors, *Physica C* **176** 95 (1991).

15 J L Tallon, C Bernhard, H Shaked, R L Hitterman and J D Jorgensen, Generic superconducting phase behavior in high-T_c cuprates: T_c variation with hole concentration in $YBa_2Cu_3O_{7-\delta}$, *Phys. Rev. B* **51** 12911 (1995).

16 J P Perdew, K Burke and M Ernzerhof, Generalized gradient approximation made simple, *Phys. Rev. Lett.* **77** 3865 (1996).

17 V I Anisimov, J Zaanen and O K Andersen, Band theory and Mott insulators: Hubbard U instead of Stoner I, *Phys. Rev. B* **44** 943 (1991). doi:10.1103/PhysRevB.44.943

18 S L Dudarev, G A Botton, S Y Savrasov, C J Humphreys and A P Sutton, Electron-energy-loss spectra and the structural stability of nickel oxide: an LSDA+U study, *Phys. Rev. B* **57** 1505 (1998).

19 M Cococcioni and S de Gironcoli, Linear response approach to the calculation of the effective interaction parameters in the LDA+U method, *Phys. Rev. B* **71** 035105 (2005).

20 G Makov and M C Payne, Periodic boundary conditions in ab initio calculations, *Phys. Rev. B* **51** 4014 (1995).

21 P Giannozzi *et al*, QUANTUM ESPRESSO: a modular and open-source software project for quantum simulations of materials, *J. Phys.: Condens. Matter* **21** 395502 (2009). doi:10.1088/0953-8984/21/39/395502

22 P Giannozzi *et al*, Advanced capabilities for materials modelling with Quantum ESPRESSO, *J. Phys.: Condens. Matter* **29** 465901 (2017).

23 A P Thompson *et al*, LAMMPS – a flexible simulation tool for particle-based materials modeling at the atomic, meso, and continuum scales, *Comput. Phys. Commun.* **271** 108171 (2022).

COLOPHON

How this document was made

The Kronos Fleet — Combined Editorial, 2026 is set in **Fraunces** (display), **Gelasio** (text), and **IBM Plex Mono** (data & equations), carried forward from the Kronos editorial design system.

The figures are rendered at 300 dpi from the deposited generator scripts; the document is composed as a single self-contained file with embedded fonts and imagery, paginated to US Letter, and rendered to PDF through a headless Chromium engine in matched light and dark editions.

Every headline quantity carries an evidence class; withdrawn and restated values are marked as such. Nothing herein is frozen beyond the founder-approved Tier-A set.

Explore it live — turn the interactive 3-D model, run the deposited solvers in the physics validator, and watch the companion film series.

LEGAL NOTICE

Notice, status, and distribution

Conceptual design & simulation study. This document reports a conceptual design and simulation study. It is not a construction commitment, a safety-analysis report, a regulatory filing, or an offer of securities. Forward-looking statements — schedules, costs, market sizes, and performance — are estimates subject to the limitations set out in the Simulations part and may change.

Numbers and their classes. Quantities are reported with evidence classes and case labels; modelled, assumed, and requirement-class values are identified as such and are not to be quoted without their labels.

Public edition. This edition carries the physics and design only; all financial, funding, and defense-commercial content has been removed for public distribution. The scientific text corresponds to the arXiv and journal submissions.

THE 2026 KRONOS SERIES

One programme, many papers

This editorial is one paper in the Kronos 2026 series — a real fusion company's complete, reproducible physics record for a spherical-tokamak breeder and its low-neutron D–^{3}He tandem-mirror burners. Every headline number is a frozen anchor in the Physics De-Risking Register.

Explore the whole programme: the De-Risking Register, the interactive 3-D model, and the physics validator.

KRONOS FUSION ENERGY

First-Principles Radiation Tolerance of Centrepost REBCO in a Compact Spherical-Tokamak Breeder: Chain-Oxygen-Vacancy Formation by DFT+U and YBCO Displacement-Cascade Molecular Dynamics

A real fusion company building real machines. Explore the science, live.

Zenodo · doi:10.5281/zenodo.22645923

Read on kronosfusionenergy.com

The Physics De-Risking Register